UNIVERSITY OF WEST BOHEMIA

Applied and Computational Mechanics 2 (2008) 291–302

Applied and Computational Mechanics

Mechanical behavior of fabric-reinforced elastomer straight flexible hoses

P. Y. Manach[a,*]

[a] *Université Européenne de Bretagne, LIMATB, Université de Bretagne-Sud, Lorient, France*

Received 18 August 2008; received in revised form 17 October 2008

Abstract

This paper presents a model applicable to large strain analysis of composite materials such as flexible hoses. A three-dimensional constitutive law, which uses the concept of convected coordinate frame, is developed for materials presenting non linear elastic and linear orthotropic behaviors in the large deformation field. The proposed model is implemented in a finite element home code and the formulation of both the hyperelastic and the orthotropic constitutive laws is presented. Finally, in order to validate our numerical results, an experimental device is developed to exhibit the mechanical behavior of straight flexible hoses in the case of elementary tests. The model is then compared to these experimental results.

Keywords: Orthotropy, Hyperelasticity, Fabric-reinforced rubber, Flexible hose

1. Introduction

In service, flexible hoses are generally submitted to low internal pressure, as well as to full travel and angular movements in all the directions. Therefore, the behavior of such materials involves a great deal of deformation complex modes and the modeling of this behavior goes through a knowledge of elementary behaviors. For example, in the case of flexible hoses made out of fabric-reinforced elastomer it is necessary to take into account both the non-linear quasi-reversible behavior of the rubber and the elastic orthotropic behavior of the fabric.

Many papers published in the literature have dealt with the global analysis of flexible hoses and pipes as reviewed in [1] or [2], and most of the numerical analysis of these highly non-linear slender structures using the finite element method [3, 4, 5, 6, 7, 8]. The finite element method is perhaps the most widely adopted technique due to its versatility in handling complex flexible pipe profile and boundary conditions. The traditional framework of large transformations is usually adopted in the conventional finite element method as it allows for a convenient way to express the governing equations and the constitutive laws in a simple form. This paper presents an alternative but more effective flexible hose formulation using 3D finite elements which can take internal pressure effect, bending-torsion coupling, axial-radial coupling, etc. into account.

A first step of our study consisted in the development and the implementation in a finite element code of an hyperelastic constitutive law [9, 10, 11] to model the large deformations of the silicon elastomer matrix. To complete the model, an orthotropic constitutive law was used to describe the behavior of the reinforcement fabrics [12]. This convected orthotropic constitutive law is introduced in a finite element code. This code has the particularity of dealing intrinsically

*Corresponding author. Tel.: (33) 297 874 571, e-mail: Pierre-Yves.Manach@univ-ubs.fr.

with large strains by using a system of material coordinates convected by the displacement of the body. In order to compare our numerical results, an experimental device was developed to exhibit the mechanical behavior of straight flexible hoses in the case of elementary tests such as tension, compression, bending or torsion. The originality of this work consists in the combination of both non linear hyperelastic and linear orthotropic constitutive laws to describe the behavior of complex material structures such as flexible hoses, and its comparison with well-established experimental results.

In the first part of this paper, the materials as well as the experimental device are described. In the second part, the theoretical formulation of the model is reviewed; convected material coordinates are presented, as well as the formulation of 3D kinematics. Both the hyperelastic and the orthotropic constitutive laws are presented and their integration into a finite element approach by the use of the variational formulation is also described. In the last part, the model is compared to experimental results obtained on straight flexible hoses.

2. Experimental

The flexible hoses are composed of a rubberized polyester fabric embedded between two silicon elastomer layers, each of the three layers being $2\,\text{mm}$ thick (see Fig. 1). All material parameters are identified by inverse optimization with the software SiDoLo [13]. The mechanical properties of the elastomer layers are determined from tensile tests in order to determine the material parameters of the hyperelastic constitutive law. Those of the rubberized fabric layer are obtained from tensile tests as well as from shear tests since the chosen constitutive behavior is orthotropic. Each type of test is performed at least three times to ensure good reproducibility of the experiments.

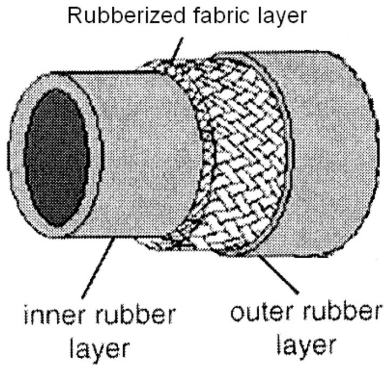

Fig. 1. Schematic drawing of the straight flexible hoses

2.1. Silicon elastomer

As the behavior of elastomers is usually considered as isotropic [14], the material parameters are identified by tensile tests alone. The samples are bone-shaped specimens of $100\,\text{mm}$ gauge length and $2\,\text{mm}$ thick. The results obtained on two different samples are presented Fig. 2. From these curves, the Cauchy stress-Almansi strain curves are calculated using the relation: $2\epsilon = (l^2 - l_0^2)/l^2$ where l_0 and l are the initial and the current gauge length of the extensometer respectively. The bulk modulus k is obtained by the relation: $k = E/3(1-2\nu)$, where $E =$

$3(\mu_r+\mu_\infty)$ and $\nu = 0.47$ are the Young modulus and the Poisson's ratio respectively. From these results, the material parameters which are obtained by identifying the hyperelastic constitutive law [10, 11] are given in Table 1.

Table 1. Material parameters of the silicon elastomer layers (in MPa)

k	Q_0	μ_r	μ_∞
250	0.94	0.055	0.015

2.2. Rubberized fabric

The rubberized fabric layer is made of a polyester fabric woven at $90°$ and cast into a silicon elastomer layer. For tensile tests, the sample has the same shape and dimensions as for elastomeric ones. As this layer is modeled using an orthotropic constitutive law, the principal fiber directions of the fabric are tested, i.e. $0°$ and $90°$, the tensile test results being presented Fig. 2 which show that the behavior is strongly non-isotropic.

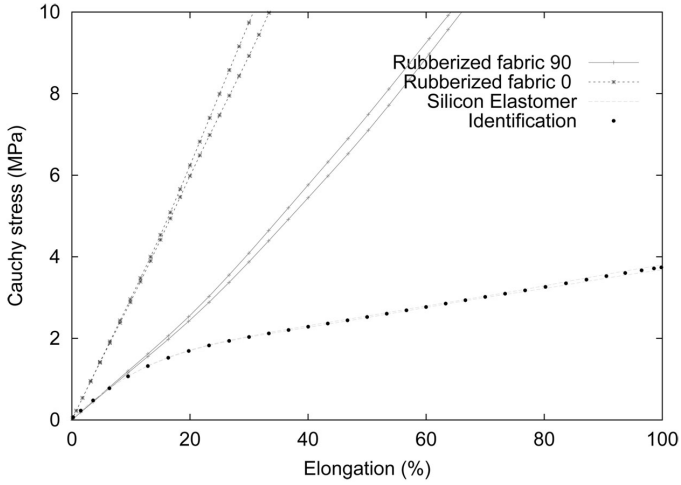

Fig. 2. Tensile tests performed on silicon elastomer samples and on rubberized fabric samples at $0°$ and $90°$ orientation with respect to the fiber directions of the fabric. Identification of the elastomer's behavior using parameters of Table 1

The shear modulous G_{12} in the layer plane is determined from shear tests using the experimental device presented in [15]. The Poisson's ratio ν_{12} is taken as the common value used for elastomer materials [14]. Finally, parameters $E_3, \nu_{13}, \nu_{23}, G_{13}, G_{23}$ of the orthotropic constitutive law are those of the silicon elastomer layer. From these results, the material parameters which are obtained by identifying the orthotropic constitutive law [12] are given in Table 2.

Table 2. Material parameters of the rubberized fabric layer (E_1, E_2 and G_{12} are in MPa)

E_1	E_2	ν_{12}	G_{12}
30.25	15.32	0.47	12.56

2.3. Experimental device

An experimental device has been developed for testing straight flexible hoses under elementary tests such as tension, compression, bending and torsion. Because the strains generated by the internal pressure in service ($P = 0.12$ MPa) are rather weak compared to those generated by full travels and angular movements, the mechanical tests are performed without internal pressure. The device is connected to a tensile machine of maximum load capacity of 100 kN. The measurement of the force is performed by a load cell of maximum capacity of 5 kN and the measurement of the displacement is directly given by the movable crosshead. The displacement rate is 5 mm/min.

For tensile and compression tests, the flexible hoses are set on each side in two striated adapters tightened by a flexible collar. For bending tests, the experimental device, presented in Fig. 3a, allows one to test two flexible hoses together. A U-shaped plateau is connected to the movable crosshead of the tensile machine. On the lateral parts of this plateau, two flexible hoses are tightened using the same adapters that are used for tensile tests. In the central axis, both flexible hoses are clamped using tensile adapters which are directly connected to the fixed crosshead of the tensile machine, see Fig. 3a. Then, when moving the plateau with respect to the central axis, a clamped-clamped bending is obtained on the flexible hoses.

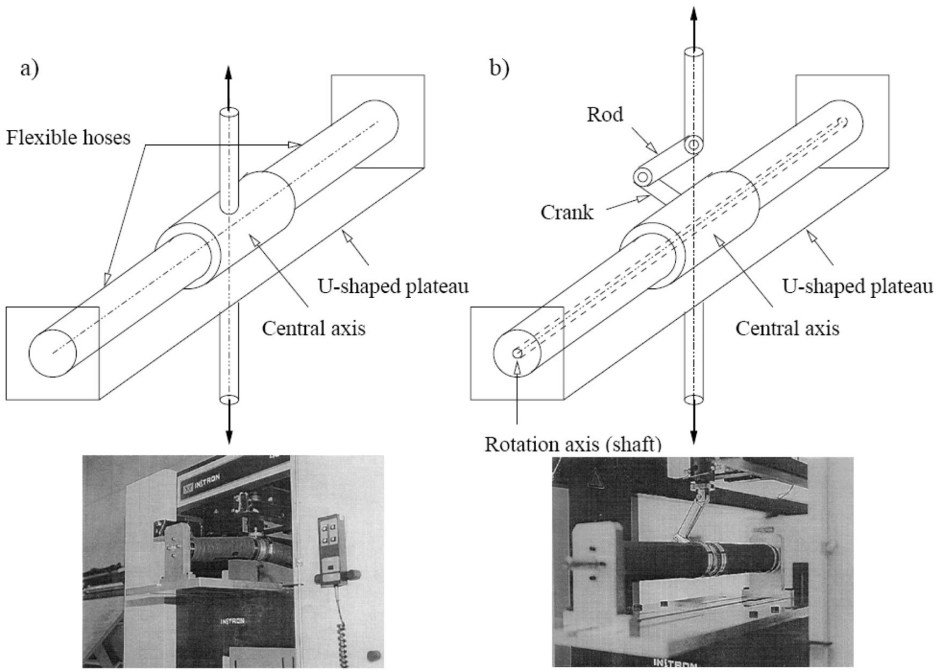

Fig. 3. Experimental device for the test of elementary behavior of straight flexible hoses. a) bending test and b) torsion test

For torsion tests, the device is similar to the previous one, except for the central axis, see Fig. 3b. A shaft (rotation axis) is inserted between the lateral parts of the U-shaped plateau and the central axis is connected to this shaft by two ball bearings. The rotation motion of the central axis is performed from the linear displacement of the tensile machine by a rod and crank system. The flexible hoses are also clamped using tensile adapters and a flexible collar.

3. Constitutive behavior

The mechanical behavior of the elastomer layers is modeled using a hyperelastic constitutive law which has already shown its ability to accurately describe the behavior of rubber-like materials. Concerning the rubberized fabric, if large deformations are considered, classical orthotropic behavior can no longer be retained because of the loss of material symmetry. In order to keep a single law, even for large deformations, the concept of convected orthotropy has been introduced [12]. This general framework has also been used to define other constitutive laws such as elastohysteresis [9] and their application to shape memory alloys and elastomers [16, 17, 10]. This section presents a review of the model.

3.1. Kinematics

The theoretical formulation of the model is written considering large geometrical transformations including large deformations. In that context, a general 3D kinematics involving convected material frames is studied according to Green and Zerna [18]. Let us consider a continuous body Ω in motion and M a point on this body. The position of M is defined in a fixed cartesian frame $\vec{I}_a$, $a = 1, 2, 3$ by its coordinates $X^a_{(0)}$ at time $t = 0$ and $X^a_{(t)}$ at time $t > 0$. To follow the point M in its motion, it is marked using curvilinear coordinates θ^i, $i = 1, 2, 3$. This marking is constant throughout the deformation and the simplest one is the coordinates in the fixed frame at $t = 0$. In the simulation and for the sake of simplicity, the curvilinear coordinates are equal to the coordinates on the reference element. A corresponding natural frame $(M, \vec{g}_i)$ is associated with point M:

$$\vec{g}_{i(t)} = \frac{\partial \vec{M}_{(t)}}{\partial \theta^i} = \frac{\partial X^a_{(t)}}{\partial \theta^i} \vec{I}_a \tag{1}$$

The $\vec{g}_{i(t)}$ vectors are calculated at time t and they evolve during the deformation. The covariant components of the metric tensor $\boldsymbol{G} = g_{ij(t)}\, \vec{g}^{\,i}_{(t)} \otimes \vec{g}^{\,j}_{(t)}$ are derived from these vectors: $g_{ij(t)} = \vec{g}_{i(t)} \cdot \vec{g}_{j(t)}$, where the contravariant or dual vectors $\vec{g}^{\,i}_{(t)}$ are defined as follows: $\vec{g}^{\,i}_{(t)} \cdot \vec{g}_{j(t)} = \delta^i_j$. Finally, the Almansi strain tensor $\boldsymbol{\epsilon}$, which is expressed in the final configuration, is calculated from:

$$\boldsymbol{\epsilon} = \frac{1}{2} \left(g_{ij(t)} - G_{ij(0)} \right) \vec{g}^{\,i}_{(t)} \otimes \vec{g}^{\,j}_{(t)} \tag{2}$$

For the remaining part of this paper, the subscripts t and 0 are omitted and the convected material vectors at $t = 0$ are referred using capital letters.

3.2. Hyperelastic constitutive behavior

For an isotropic body, the hyperelastic stress is determined from the elastic energy density E (per unit of deformed body), that is for an isothermal reversible transformation, the Helmholtz free energy. By denoting $g = \det |g_{ij}|$, the hyperelastic stress contribution $\boldsymbol{\sigma}_r$ can be defined from the internal energy:

$$\boldsymbol{\sigma}_r : \boldsymbol{D} = \frac{1}{\sqrt{g}} \frac{\partial (\sqrt{g}\, E)}{\partial t} \tag{3}$$

where $\boldsymbol{D}$ is the strain rate tensor and t the current time. The elastic energy is supposed to be a function of the strain state of the material and the strain tensor $\boldsymbol{\epsilon}$ is chosen to represent this state. This leads to:

$$\boldsymbol{\sigma}_r : \boldsymbol{D} = \sigma^{ij} D_{ij} = \frac{1}{\sqrt{g}} \frac{\partial (\sqrt{g} E)}{\partial \epsilon_{ij}} \frac{\partial \epsilon_{ij}}{\partial t} \tag{4}$$

The previous expression is valid if the strain rate tensor components are written in the convected material frame, i.e. $\boldsymbol{D} = \partial\epsilon_{ij}/\partial t\, \vec{g}^{\,i} \otimes \vec{g}^{\,j}$. By identification, the hyperlastic stress contribution can be deduced from the variations of the elastic energy density:

$$\frac{\partial(\sqrt{g}\, E)}{\partial \epsilon_{ij}} = \sqrt{g}\, \sigma^{ij} \tag{5}$$

If the body is assumed to be isotropic, the hyperelastic stress is determined from the elastic energy density E which depends only on three strain invariants. Macroscopically, the choice of the intensity of the deviatoric strain tensor $\overline{II}_{\bar{\epsilon}}$ as a first variable is thus physically meaningful [19]. The set of variables is completed by the ratio of elementary volumes $v = \sqrt{g/G}$, where $G = \det|G_{ij}|$ and by the phase of the deviatoric strain tensor $\varphi_{\bar{\epsilon}}$ such as:

$$\cos(3\varphi_{\bar{\epsilon}}) = \frac{3\sqrt{3}}{2} \frac{\overline{III}_{\bar{\epsilon}}}{\overline{II}_{\bar{\epsilon}}^{3/2}} \tag{6}$$

where $\overline{III}_{\bar{\epsilon}}$ is the third invariant of the deviatoric strain tensor. The following expression has been chosen because it gives satisfying results for elastomer materials:

$$E = \frac{k_r \ln^2 v}{6} + \frac{Q_r^2}{2\mu_r} \ln\left[\cosh\left(\frac{2\mu_r}{Q_r}\sqrt{2\overline{II}_{\bar{\epsilon}}}\right)\right] + 2\mu_\infty \overline{II}_{\bar{\epsilon}} \tag{7}$$

where k_r, Q_r, μ_r and μ_∞ are the parameters of this law. k_r is proportional to the bulk modulus while $(\mu_r + \mu_\infty)$ represents the initial slope on a graph of shear stress against shear strain curve and Q_r an elastic threshold. A complete description of this law as well as the definition of the parameters of the law can be found in [10, 11].

3.3. Orthotropic constitutive behavior

In the case of fabric materials, finite deformations can appear by twisting in the fiber plane without any large deformations in the direction of the fibers. The deformed material is no longer orthotropic, unless the initial behavior is the same in the main direction of the fibers. In accordance with the classical elasticity theory, these remarks lead to an anisotropic behavior defined with 21 coefficients. Anyway, it appears that the behavior along the directions corresponding to the initial main directions convected on the deformed body does not change much. This is the main idea used here to define the evolution of the initial orthotropy. The model obtained allows us to keep only the 9 initial parameters from the general orthotropic behavior [12].

Let us consider a field of objectively defined frame which is initially the orthonormal field associated with the directions of material anisotropy. This field is convected associated with the dragged-along material coordinates [20]. This material frame of unit vectors $\vec{O}_i$ $(i = 1, 2, 3)$ whose direction coincide with the initial direction of the fabric fibers and represents the orthotropic main directions of the body with regard to the fixed reference frame $\vec{I}_a$. The relation between the initial orthotropic frame and the natural frame $\vec{g}_{i(t)}$ can be defined by a rotation of angle α in the tangent plane to the medium surface of the element. The orthotropic constitutive behavior is still represented by a non constant 4th-order tensor $\boldsymbol{E}$ such as:

$$\boldsymbol{\sigma} = \boldsymbol{E} : \boldsymbol{\epsilon} \tag{8}$$

where $\boldsymbol{\sigma}$ is the Cauchy stress tensor. In the initial condition, the coordinates of $\boldsymbol{E}$ in the $\vec{O}_i$ frame can be represented by the classical matrix of orthotropic elasticity, obtained by inverting

the stiffness matrix $\boldsymbol{S}$ for which terms are generally simpler. In accordance with our previous assumption, the coordinates of $\boldsymbol{E}$ are assumed constant during deformation and the tensor $\boldsymbol{E}$ is written in the initial orthotropic frame $\vec{O}_i$:

$$\boldsymbol{E} = E^{i}{}_{jk}{}^{l}\ \vec{O}_i \otimes \vec{O}^j \otimes \vec{O}^k \otimes\ \vec{O}_l \tag{9}$$

where $i, j, k, l = 1, 2, 3$. The constitutive law is then obtained in mixed coordinates (contravariant and covariant) in the orthotropic frame since the mixed frame is the only frame where stresses and strains remain of the same magnitude than $\vec{I}_a$. However, all the terms of the constitutive law should be written in the same frame, such as:

$$\sigma^{ij} = E^{ijkl}\ \epsilon_{kl} \tag{10}$$

In our case, it is necessary to calculate the covariant coordinates of $\boldsymbol{E}$ in the natural frame. Moreover, the frame in which this relation is expressed has to be normalized since the $\vec{O}_i$ vectors are deformed similarly to the $\vec{G}_i$ vectors. In the original condition, the $\vec{O}_i$ vectors are defined by:

$$\vec{O}_i = A_i^{\ j}\ \frac{\vec{G}_j}{||\vec{G}_j||} \qquad \text{and} \qquad \vec{O}^{\,j} = B^j_{\ i}\ \frac{\vec{G}^{\,i}}{||\vec{G}^{\,i}||} \tag{11}$$

where $(i, j = 1, 3)$. The convected orthotropy hypothesis leads to coefficients $\boldsymbol{A}$ and $\boldsymbol{B}$ which remain constant during the deformation, i.e. the orthotropic frame follows the rotation of the natural frame; this gives in the deformed condition:

$$\vec{o}_i = A_i^{\ j}\ \frac{\vec{g}_j}{||\vec{g}_j||} \qquad \text{and} \qquad \vec{o}^{\,j} = B^j_{\ i}\ \frac{\vec{g}^{\,i}}{||\vec{g}^{\,i}||} \tag{12}$$

Let use define the following terms:

$$\Gamma_{\alpha}^{\ \beta} = \frac{\vec{o}_\alpha}{||\vec{o}_\alpha||} \cdot \vec{g}^{\,\beta} \qquad \text{and} \qquad \Lambda^{\beta}_{\ \alpha} = \frac{\vec{o}^{\,\beta}}{||\vec{o}^{\,\beta}||} \cdot \vec{g}_\alpha \tag{13}$$

Tensor $\hat{\boldsymbol{E}}$ in the deformed natural frame $\vec{g}_i^{\,'} = \vec{g}_i / ||\vec{g}_i||$ is then expressed as:

$$\begin{aligned} \hat{\boldsymbol{E}} &= E^{i}{}_{jk}{}^{l}\ \Gamma_i^{\ \alpha}\, \Lambda^j_{\ \beta}\, \Lambda^k_{\ \gamma}\, \Gamma_l^{\ \delta}\, g^{\beta\beta'}\, g^{\gamma\gamma'}\ \vec{g}_\alpha^{\,'} \otimes \vec{g}_{\beta'}^{\,'} \otimes \vec{g}_{\gamma'}^{\,'} \otimes \vec{g}_\delta^{\,'} \\ &= E^{\alpha\beta'\gamma'\delta}\ \vec{g}_\alpha^{\,'} \otimes \vec{g}_{\beta'}^{\,'} \otimes \vec{g}_{\gamma'}^{\,'} \otimes \vec{g}_\delta^{\,'} \end{aligned} \tag{14}$$

where $\alpha, \beta, \beta', \gamma, \gamma', \delta = 1, 2, 3$. The initial material frame $\vec{G}_i$ is known from the finite element discretization and the initial position of the orthotropic frame $\vec{O}_i$ is determined from the initial orientation of the fibers of the fabric with respect to the material frame. The material parameters introduced in $\boldsymbol{E}$ are also known and kept constant during the deformation, but both material and orthotropic frames evolve during the deformation. All other quantities are computed.

3.4. Variational formulation

The weak formulation of the boundary-value problem, defined both by the boundary conditions and the equilibrium equations derived from the principle of virtual power is written in the final configuration:

$$\int_\Omega \sigma^{ij}\ \overset{*}{v}_i\ |_j\, \mathrm{d}\Omega = \int_\Sigma t^i\ \overset{*}{v}_i\ \mathrm{d}\Sigma \tag{15}$$

where $\vec{t}$ represents the surface external force. The previous relation must be fulfilled for virtual velocity field $\overset{*}{\vec{v}}$ resulting from any kinematically admissible displacement field. From the finite element discretization, and taking into account that the virtual velocity field is arbitrary in the volume Ω and on the surface Σ, this leads in a standard way to the system of algebraic non-linear equations:

$$R_{bs}\left(X^{ar}\right) = 0 \qquad \forall b, s \tag{16}$$

with:

$$R_{bs}\left(X^{ar}\right) = \sum_{n=1}^{ne} \left[\int_{\Omega_n} \sigma^{ij} \, \frac{\partial D_{ij}}{\partial X^{bs}} \, \mathrm{d}\Omega_n - \int_{\Sigma_n} t^i \, \frac{\partial X_i}{\partial X^{bs}} \, \mathrm{d}\Sigma_n \right] \tag{17}$$

where X^{ar} are nodal positions, ne is the number of elements, and where Ω_n and Σ_n are related to element n. The previous system is then solved using a Newton-Raphson method. In that respect, it is necessary to determine the stiffness of the system, i.e. the tangent linear form with respect to the degrees of freedom. The variations of different geometrical terms with respect to the degrees of freedom can be obtained in [10] for the hyperelastic constitutive law and in [12] for the orthotropic constitutive law.

4. Results

This part is devoted to the validation of the model presented in the previous part. The validation of the orthotropic behavior has already been performed in the small deformation field: firstly, the different elementary behaviors of orthotropic laminates have been compared to the theoretical results obtained in the small strain field [12]. Secondly, the bending behavior of an orthotropic laminate under a sinusoidal loading of Pagano type has been compared to the Pagano's solution [21]. Both first points correspond well with theoretical results [12]. In this paper, the complete model is compared to several experimental cases of straight flexible hoses submitted to elementary tests. It can be noted that for all simulations, the influence of the mesh has been previously studied and that the results presented are obtained with a sufficiently fine mesh to ensure stable solutions.

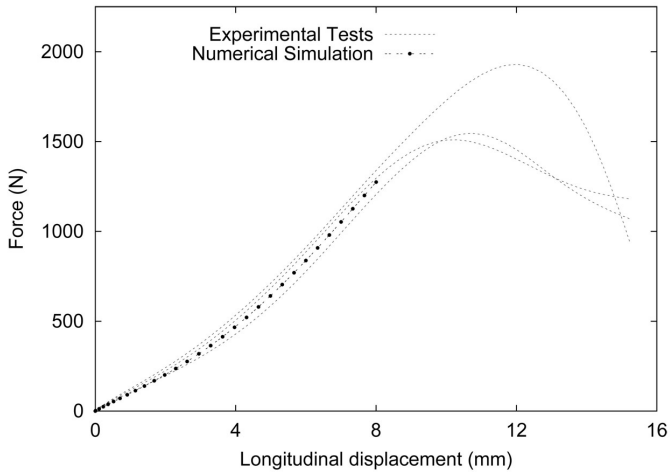

Fig. 4. Experimental and numerical results obtained on straight flexible hoses under tension tests

The flexible hoses are composed of three layers of equal thickness 2 mm, i.e. one layer of rubberized fabric embedded in two layers of silicon elastomer. The initial orientation of the fabric is 45° with respect to the lengthwise direction, see Fig. 1.

The dimensions are 170 mm length, with 100 mm of gauge length and 35 mm on each lateral side for the clamped part of the flexible collar, an inner diameter of 58 mm and a total thickness of 6 mm. Two layers of quadratic hexaedron elements represent each layer of the flexible hose. The mesh is composed of 100 elements in the length, 6 in the thickness and 36 on the circumference. The $\vec{z}$ axis is taken lengthwise to the hose while $\vec{x}$ and $\vec{y}$ are located in a section, the origin of the frame is taken on the left side of the mesh. Boundary conditions obviously depend on the type of test but for all cases, the first row of elements on one side is completely fixed, i.e. $u = v = w = 0$ because it represents the first clamped part of the hose. For tension or compression tests, the first row on the other side represents the other clamped part at the flexible collar, which means that $u = v = 0$. For tension tests $w > 0$ and for compression tests $w < 0$. For bending tests, the first row on the other side is such that $u = w = 0$ and $v > 0$, i.e. a displacement to a cross direction. Finally, for torsion tests, two lateral parts have been added to the previous mesh in order to create a torque around the $\vec{z}$ axis by applying a pressure on these lateral parts.

The results presented Fig. 4, Fig. 5, Fig. 6, Fig. 7 feature the curves obtained in the different cases of tests. For each test, three samples have been tested to ensure the reproductibility of the results. It can be observed that there is a good accordance between experimental curves and simulated results even for finite deformations. In all other cases than tension, the results are performed for strains so that there are no buckling effects. For compression tests, simulated results obtained using parameters of Table 1 show a discrepancy between experimental and numerical results (see Fig. 5 (Numerical Simulation 1)).

This is due to the fact that this test is performed using the same material parameters in tension and in compression while the behavior of the elastomer is not symmetric for these tests. In order to take non-symmetric behavior in tension and compression into account, a dependence on $\varphi_{\bar{\epsilon}}$ is added through the material parameter $Q_0(\varphi_{\bar{\epsilon}})$ which replaces the parameter Q_0. The

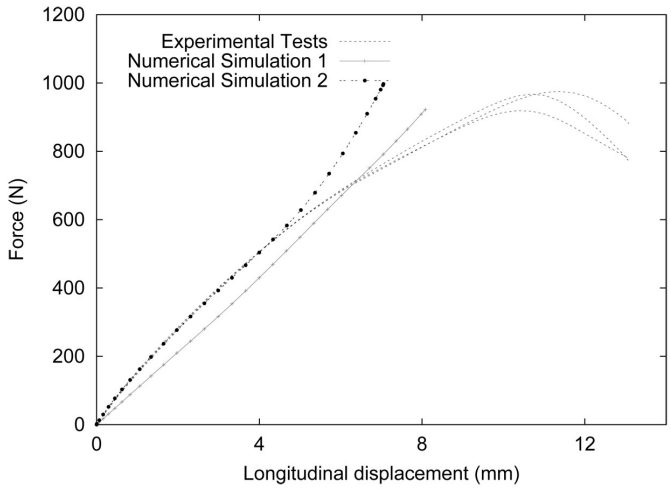

Fig. 5. Experimental and numerical results obtained on straight flexible hoses under compression tests

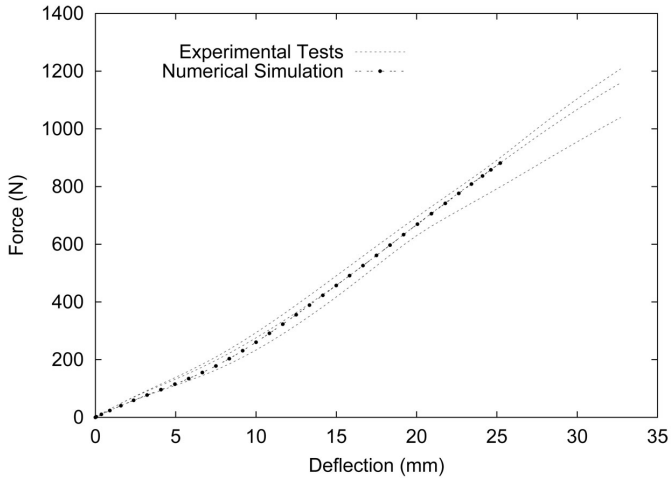

Fig. 6. Experimental and numerical results obtained on straight flexible hoses under flexion tests

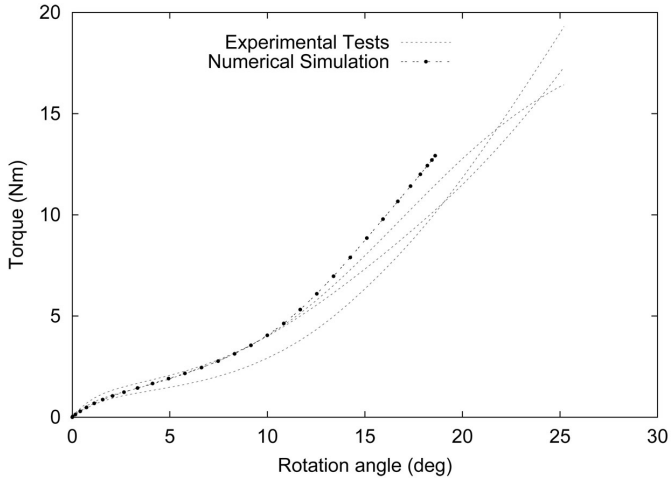

Fig. 7. Experimental and numerical results obtained on straight flexible hoses under torsion tests

following relation is used:

$$Q_0 = \frac{Q'_0}{(1 + \gamma \cos 3\varphi_{\bar{\epsilon}})^n} \tag{18}$$

where Q'_0, γ, n are parameters characteristic of the material. It gives a different threshold in tension ($\varphi_{\bar{\epsilon}} = 0$) and in compression ($\varphi_{\bar{\epsilon}} = \pi/3$), thus leading to a non-symmetric behavior. The results obtained using these parameters are presented in Fig. 5 (Numerical Simulation 2). The agreement between experimental and numerical results is then satisfying for a large range of deformation. For torsion tests, the results are initially obtained in terms of rod displacement vs load. In order to transform these curves in rotation angle vs torque, the following relation is used:

$$\alpha = \frac{1}{l\lambda^2}\left(-r + \sqrt{r^2 - \frac{l\lambda^2}{2}(l\lambda^2 + 4r + l\lambda^2\Delta l)}\right) \tag{19}$$

where r is the crank's length, l is the rod's length, $\lambda = r/l$ and α is the rotation angle. These numerical results correspond well with experimental ones. Numerical simulations of more complex shapes of flexible hoses submitted to both internal pressure and full travel movements are in progress.

5. Conclusions

This paper deals with a study of mechanical behavior of straight flexible hoses submitted to elementary tests such as tension, compression, bending and torsion. An experimental device has been developed in order to obtain experimental results in the finite deformation field. A model has been proposed and implemented in a finite element code to simulate the experimental results. This model uses convected material frames and the constitutive behavior is described by both a hyperelastic law for elastomer layers of the hose and an orthotropic law for the rubberized fabric layer. This model is compared to experimental results obtained on straight flexible hoses and the results correspond well even for large deformations.

Acknowledgements

The author thanks the company Avon Polymères France for financial support.

References

[1] H. M. Patel, F. B. Seyed, Review of flexible riser modeling and analysis techniques. Engineering structures, 17 (1995) 293–304.

[2] Y. T. Chai, K. S. Varyani, An absolute coordinate formulation for three-dimensional flexible pipe analysis. Ocean Engineering, 33 (2006) 23–58.

[3] D. G. Owen, K. Qin, Model tests and analysis of flexible riser systems. In: Proceedings of the 5th International Conference on Offshore Mechanics and Artic Engineering, Tokyo, Japan, 1986.

[4] H. Vogel, B. J. Natvig, Dynamics of flexible hose riser systems. Journal of Offshore Mechanics and Aric Engineering, 3 (1987) 244–248.

[5] P. G. Bergan, Non-linear finite element analysis by use of Fenris. In: Proceedings of the 7th International Seminar on Computational Aspects of Finite Element Method CAFEM 7, Chicago USA, 1983.

[6] J. F. McNamara, P. J. O'Brien, S. G. Gilroy, Non-linear analysis of flexible risers using hybrid finite elements. Journal of Offshore Mechanics and Aric Engineering, 110(3) (1988) 197–204.

[7] J. R. Cho, J. I. Song, K. T. Noh, D. H. Jeon, Nonlinear finite element analysis of swaging process for automobile power steering hose. Journal of Materials Processing Technology, 170 (2005) 50–57.

[8] H. Baaser, Global optimization of length and macro-micro transition of fabric-reinforced elastomers with application to a brake hose. Computational Materials Science, 39 (2007) 113–116.

[9] G. Rio, P. Y. Manach, D. Favier, Finite element simulation of 3D mechanical behavior of NiTi shape memory alloys. Archives of Mechanics, 47 (1995) 537–556.

[10] C. Moreau, S. Thuillier, G. Rio, V. Grolleau, The mechanical behavior of a slightly compressible rubber-like material: correlation of simulations and experiments. Rubber Chemistry and Technology, 2 (1999) 269–282.

[11] D. Favier, G. Rio, P. Y. Manach, Grandes deformations et lois d'elastohysteresis appliquees au calcul par elements finis d'elastomeres. In: Proceedings of the Colloque International Francophone de Génie Mécanique des Caoutchoucs et des Elastomères Thermoplastiques, Nancy France, 1997, 327–330.

[12] P. Y. Manach, G. Rio, Analysis of orthotropic behavior in convected coordinate frames. Computational Mechanics, 23 (1999) 510–518.

[13] P. Pilvin, Identification des paramètres de modèles de comportement. International Seminar on the inelastic behavior of solids Mécamat, Besançon, France, (1988) 155–161.

[14] D. J. Charlton, J. Yang, K. K. Teh, A review to characterize rubber elastic behavior for use in finite element analysis. Rubber chemistry and technology, 67 (1994) 481–503.

[15] P. Y. Manach, D. Favier, Shear and tensile thermomechanical behavior of near equiatomic NiTi alloy. Materials Science and Engineering, A222 (1997) 45–57.

[16] P. Y. Manach, D. Favier, G. Rio, Finite element simulations of internal stresses generated during the ferroelastic deformation of NiTi bodies. Journal de Physique IV, C4 (1995) 235–244.

[17] G. Rio, D. Favier, H. Desplats, Finite element simulation of mechanical behavior of shape memory alloys coupled with a non-stationary thermal field. Journal de Physique IV, C5 (1995) 215–220.

[18] A. E. Green, W. Zerna, Theoretical elasticity. 2nd Edition, Oxford University Press, 1968.

[19] D. Favier, P. Guélin, P. Pégon, Thermomechanics of hysteresis effects in shape memory alloys. In: Proceedings of the International Conference on Martensitic Transformation, Sydney Australia (1989) 559–564.

[20] P. Pegon, P. Guelin, Finite strain plasticity in convected frames. International Journal for Numerical Methods in Enginneering, 22 (1986) 521–545.

[21] N. J. Pagano, Exact solutions for rectangular bidirectional composite and sandwich plates. Journal of Composite Materials, 4 (1970) 20–35.